Journal of Alloys and Compounds 845 (2020) 156188

Contents lists available at ScienceDirect

Journal of Alloys and Compounds

journal homepage: http://www.elsevier.com/locate/jalcom

Influence of the order of fabrication sequences on the thermoelectric properties of skutterudite $CoSb_3$—$Cu_{0.6}Ni_{0.4}$ nanocomposites

Ahmad Gharleghi [a, *], Md Mobarak Hossain Polash [b, c], Rasoul Malekfar [a], Sima Aminorroaya Yamini [d], Daryoosh Vashaee [b, c, **]

[a] Department of Physics, Faculty of Basic Science, Tarbiat Modares University, Tehran, I.R, Iran
[b] Department of Materials Science and Engineering, North Carolina State University, Raleigh, NC, 27606, USA
[c] Department of Electrical and Computer Engineering, North Carolina State University, Raleigh, NC, 27606, USA
[d] Department of Engineering and Maths, Sheffield Hallam University, Sheffield S1, 1WB, UK

ARTICLE INFO

Article history:
Received 25 November 2019
Received in revised form
19 June 2020
Accepted 22 June 2020
Available online 30 June 2020

Keywords:
Hydrothermal synthesis
$Cu_{0.6}Ni_{0.4}$ nano alloy
Cobalt skutterudite
Fabrication sequences
Nanocomposite
Thermoelectric properties
Bipolar effect

ABSTRACT

Nanocomposite samples of $CoSb_3$-x$Cu_{0.6}Ni_{0.4}$ (x = 1, 3.5, 6, and 9 wt%) were fabricated through two different approaches to understand the influence of fabrication processes on the thermoelectric properties of $CoSb_3$ skutterudite. $CoSb_3$ matrix and $Cu_{0.6}Ni_{0.4}$ nanoalloy were synthesized separately via hydrothermal procedures. The mixtures of as-hydrothermally synthesized powders were prepared and annealed in the first method, while in the second fabrication route, $CoSb_3$ powders were initially annealed, followed by mixing with $Cu_{0.6}Ni_{0.4}$ and annealing of the composite at the same conditions. The results showed improved electrical conductivity of $CoSb_3$ compounds, which is consistent with the systematic increase of the carrier concentration upon increasing the $Cu_{0.6}Ni_{0.4}$ content. The grain boundary potential barrier mechanism was used to describe the influence of $Cu_{0.6}Ni_{0.4}$ nanoalloy on the height of the energy barrier of $CoSb_3$-x$Cu_{0.6}Ni_{0.4}$, as compared with that of pristine $CoSb_3$ synthesized using the similar hydrothermal method. The onset of bipolar thermopower reduction is shifted to higher temperatures; however, the room temperature thermopower is reduced upon increasing the content of $Cu_{0.6}Ni_{0.4}$ nanoinclusions. The sample containing 1 wt% of $Cu_{0.6}Ni_{0.4}$ fabricated through the first fabrication procedure showed the highest zT value at ~550 K.

1. Introduction

Conversion of waste heat to electrical energy using thermoelectric (TE) generators has become more prevalent in both research and industrial applications for clean energy technologies [1–3]. Conventionally, the thermal to the electrical conversion efficiency of a TE material is evaluated via its dimensionless figure-of-merit, $zT = S^2T/\rho\kappa$; thereat, T, S, ρ and $\kappa = \kappa_e + \kappa_L$ are absolute temperature, thermopower (Seebeck coefficient), electrical resistivity, and total thermal conductivity, respectively. The total thermal conductivity of semiconductor material includes electronic (κ_e) and lattice (κ_L) thermal conductivity components [4]. Various strategies have been investigated to improve the zT of TE materials, including nanostructuring and electronic structure tuning via solid solution and elemental doping on ionic sites of pristine materials [5–13]. It is known that decoupling the interdependent thermopower and electrical resistivity could be an efficient approach for boosting the power factor (S^2/ρ) [14]. Hence, decoupling the electronic parameters can be a practical strategy to achieve high zT values; however, it could be a challenging task for a single-phase thermoelectric material. Obtaining composite materials could improve the transport properties of TE materials via inducing multi-mode phonon scattering from hierarchical structures. Uniform distribution of a small amount of appropriate nano inclusion in a TE material could improve the corresponding zT value through enhancing the power factor and/or reducing κ_L [14–19]. Cobalt skutterudite is one of the promising TE materials that is extensively explored by adopting strategies such as doping, cage filling, nanostructuring, and fabricating composite compounds, aiming to improve its zT value [20–27]. It is known that the pristine $CoSb_3$

* Corresponding author.
** Corresponding author. Department of Materials Science and Engineering, North Carolina State University, Raleigh, NC, 27606, USA.
E-mail addresses: a.gharleghi@modares.ac.ir (A. Gharleghi), dvashaee@ncsu.edu (D. Vashaee).

https://doi.org/10.1016/j.jallcom.2020.156188
0925-8388/

system possesses relatively low electrical conductivity and simultaneously significant Seebeck coefficients at temperatures below the onset of the bipolar effect [28,29]. Existing intrinsic vacancies in crystal-cell is one of the attractive features of skutterudites, providing the possibility of tuning the transport properties via incorporating elements from alkali, alkaline earth group, rare-earth metals or other metals such as gallium, indium, and thallium in the cell vacancies [20,22,27]. The lattice thermal conductivity of partially-filled $CoSb_3$ is reduced due to frequent scattering of phonon on the loosely bonded void fillers [26,27]. The use of composite structures to enhance the TE properties of $CoSb_3$ has recently received more attention [30–35]. The influence of various materials such as MoS_2 [36], SiC [37], reduced graphene oxide [38], WTe_2 [39], and $FeSb_2$ [40], as an additive on the thermoelectric properties of pristine or partially-filled $CoSb_3$ have been studied. Furthermore, the role of in situ formed extra crystal phases, such as Sb_2O_3 [19], $CoSb_2O_4$ [19], and InSb [41], on enhancing phonons scattering in $CoSb_3$ structure have been studied.

In the present study, the influence of composite structures and the order of fabrication sequences on the thermoelectric properties of $CoSb_3$-x$Cu_{0.6}Ni_{0.4}$ nanocomposites are investigated. Both $CoSb_3$ powder and $Cu_{0.6}Ni_{0.4}$ nanoalloy were separately synthesized through hydrothermal processes. Hydrothermally synthesized single-phase $CoSb_3$ system possesses a relatively low electrical conductivity [39,42]; therefore, pristine $CoSb_3$ were mixed with relatively high electrically conductive materials ($Cu_{0.6}Ni_{0.4}$ nanoalloy) to enhance the electrical conductivity [43]. $CoSb_3$-x$Cu_{0.6}Ni_{0.4}$ (x = 1, 3.5, 6, and 9 wt%) nanocomposite samples were prepared through two separate procedures (P1 and P2) and all annealed in a vacuum atmosphere under the same conditions. The crystal structure, microstructure, and transport properties were characterized for all the samples. The peak power factor of 6.33 $\mu Wcm^{-1}K^{-2}$ is obtained for the sample containing 1 wt% of $Cu_{0.6}Ni_{0.4}$ nanoalloy. It is found that the total thermal conductivity of $CoSb_3$-x$Cu_{0.6}Ni_{0.4}$ samples is not the same for both sets of samples. The peak zT value of 0.23 is obtained for the sample containing 1 wt% of $Cu_{0.6}Ni_{0.4}$, while higher percentages of $Cu_{0.6}Ni_{0.4}$ nanoalloy deteriorates power factor due to significantly reduced thermopower.

1.1. Experimental procedure

1.1.1. Synthesis of $CoSb_3$ powder

$CoSb_3$ powder was synthesized using a hydrothermal procedure, reacting Sb powder with a stoichiometric amount of $CoCl_2 \cdot 6H_2O$ precursor to obtain the ratio of Sb to Co elements of 3:1. The reaction was performed in a Teflon-lined autoclave. The solution was heated from room temperature to 255 °C at a heating rate of 2.5 °C/min and hold for 12 h, followed by cooling to room temperature at the same rate. The obtained precipitate was then washed using ethanol and deionized water in sequences and dried at 80 °C for 3 h in an Argon atmosphere in a tube furnace. The final single $CoSb_3$ phase was attained upon annealing partially cold-pressed (about 3 MPa) bulks of the as-synthesized powder at 585 °C for 5h at about 10^{-5} Torr vacuum atmosphere. More details on the hydrothermal synthesis of $CoSb_3$ could be found elsewhere [42].

1.1.2. Synthesis of $Cu_{0.6}Ni_{0.4}$ powder

$Cu_{0.6}Ni_{0.4}$ nanoalloy was also synthesized using a hydrothermal procedure [43]. 5.36 mmol $CuCl_2 \cdot 2H_2O$, 3.57 mmol $NiCl_2 \cdot 6H_2O$, and 5 mL Glycerol were added to 150 mL deionized (DI) water in a Teflon cup. Glycerol was added to prevent the oxidation of Cu and/or Ni elements. The solution was then stirred for 15 min, while it was heated on a hot plate at about 50 °C. The $NaBH_4$ chemical was then used to reduce the solution. The Teflon cup containing the solution was then heated in an autoclave at 170 °C for 12 h. The obtained precipitate was then washed using DI water and ethanol in sequences and dried with the same method used for drying $CoSb_3$.

1.1.3. Fabrication of $CoSb_3$-x$Cu_{0.6}Ni_{0.4}$ nanocomposites

Nanocomposite samples of $CoSb_3$-x$Cu_{0.6}Ni_{0.4}$ with x = 1, 3.5, 6, and 9 wt% were fabricated through two different procedures. For the first set of samples that were produced through procedure number one (P1), $CoSb_3$-x$Cu_{0.6}Ni_{0.4}$ nanocomposites with x = 1, 3.5, 6, and 9 wt% are labeled as sample #1 to #4, respectively. For the second set of samples that were produced through procedure number two (P2), the $CoSb_3$-x$Cu_{0.6}Ni_{0.4}$ nanocomposites with x = 1, 3.5, 6, and 9 wt% were labeled as sample #5, to #8, respectively. The first fabrication route (P1) includes mixing stoichiometric ratios of as-hydrothermally synthesized $Cu_{0.6}Ni_{0.4}$ nanoalloys with $CoSb_3$ powder and suspended in 10 mL ethanol by ultrasonication. The obtained suspension was partially dried at about 45 °C in the air followed by drying at 80 °C under argon atmosphere for 3h. The final dried powder was then partially cold-pressed at a pressure of about 3 MPa and sealed in Pyrex ampoule under 10^{-5} Torr. The sealed samples were then annealed at 585 °C for 5h.

To fabricate the second set of the samples with the same compositions through P2, we first cold-pressed the as-hydrothermally synthesized $CoSb_3$ powder and annealed it at 585 °C for 5h in an evacuated-and-encapsulated Pyrex ampoule. The annealed $CoSb_3$ was then powdered using an agate mortar and pestle and mixed with a stoichiometric ratio of as-hydrothermally synthesized $Cu_{0.6}Ni_{0.4}$ nanoalloys. To obtain a uniform suspension, we suspended the mixture in 10 mL ethanol by ultrasonication. The samples were dried using the same method used in P1. The obtained powders through both P1 and P2 were then cold-pressed into parallelepiped and disc shape samples at 17 MPa. The compacted samples were then annealed at 585 °C for 5h in a vacuum-sealed Pyrex ampoule.

Our motivation for producing $CoSb_3$-x$Cu_{0.6}Ni_{0.4}$ composites through P1 was to improve the intergrain joints of $CoSb_3$-x$Cu_{0.6}Ni_{0.4}$ particles via thermodynamically providing conditions for localizing Co and Sb ions into crystal sites of $CoSb_3$ structure and simultaneous formation of $CoSb_3$ grains with the least boundaries with that of CuNi grains, e.g., to reduce Kapitza resistance. The formation of $CoSb_3$ particles using P1 could be regarded as the in-situ formation of an extra phase inside the microstructure of the host material.

The structure of the obtained samples was analyzed using x-ray diffraction pattern (XRD). The micro-morphology of the samples was characterized using field emission scanning electron microscopy (FESEM, MIRA3-TESCAN-XMU). The thermopower (Seebeck coefficient), electrical conductivity, room temperature charge carrier concentration, and mobility measurements were carried out using a standard 4-point probe method using Linseis equipment under Helium environment. The thermopower was measured for five temperature differences at a given temperature, and each measurement was then repeated four times and then averaged. The thermopower was determined using the slope method in quasi-steady-state mode with temperature differences of 1–5 K. The temperature dependence of magnetic moment under the applied magnetic field of 10^4 emu (~0.1 T) was explored between 2 K and 400 K using vibrating sample magnetometer (PPMS, Quantum Design DynaCool). The thermal conductivity ($\kappa = D \times C_p \times \rho$) was obtained using the measured thermal diffusivity (D), specific heat capacity (C_p), and bulk density (ρ). The thermal diffusivity measurement was carried out between room temperature and 800 K in vacuum using a Laser Flash apparatus (Netzsch LFA 457 Micro

Flash) [44]. The specific heat capacity was estimated using the Dulong-Petit limit, $C_p = 3nR$; wherein n is the number of atoms per formula unit and R the universal gas constant [45]. For $CoSb_3$ matrix, $C_p = 0.235\ \frac{J}{g.K}$ was calculated, herein, $n = 32$ is the number of atoms per $CoSb_3$ cell. The C_p values $0.397\frac{J}{g.K}$ and $0.433\ \frac{J}{g.K}$ was inserted, respectively, for Cu and Ni elements [46]. The combination C_p of $CoSb_3$-x$Cu_{0.6}Ni_{0.4}$ nanocomposites could be calculated using the Kopp-Neumann rule, expressed using Eq. (1) [47].

$$C_p = \sum_{i=1}^{N} f_i C_{pi} \tag{1}$$

Where i index gets values 1 and 2 for $CoSb_3$ and $Cu_{0.6}Ni_{0.4}$ phases, respectively, and f_i being the weight percentage of a component having a specific heat capacity of C_{pi}. The bulk density of the samples was measured using the Archimedes' method.

The measurement errors for electrical conductivity, Seebeck coefficient, and thermal diffusivity are within 10%.

2. Results and discussion

2.1. Structural and morphology characterization

The XRD pattern of as-hydrothermally synthesized $Cu_{0.6}Ni_{0.4}$-nanoalloy in Fig. 1a shows that the sample formed of $Cu_{0.6}Ni_{0.4}$ phase and traces of Cu_2O phase with its most intense peak at around $2\theta \cong 38°$. The primary reflections correspond to a face-centered cubic structure with a space group of $Fm\bar{3}m$ (#225) [43]. A single phase of $Cu_{0.6}Ni_{0.4}$ nanoalloy was obtained by annealing the powder at 560 °C for 5h (Fig. 1b). The Cu_2O phase might have been reduced by residual remnant Glycerol that might have remained in the $Cu_{0.6}Ni_{0.4}$ precipitate.

Fig. 2a shows the XRD pattern of as-hydrothermally synthesized powder of $CoSb_3$, indicating that the precipitate contains Sb, CoSb, and $CoSb_2$ phases. Only traces of $CoSb_3$ phases (labeled by + symbol) could be identified in the XRD pattern of the hydrothermally synthesized precipitate, similar to previous studies [23]. Annealing the powder at 585 °C for 5h results in a single phase of $CoSb_3$ (Fig. 2b).

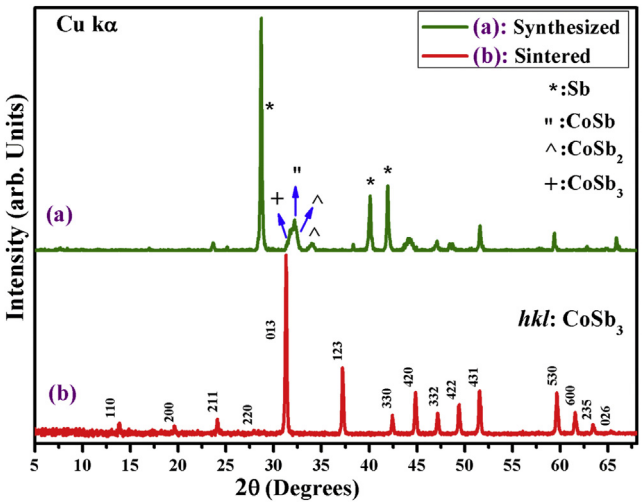

Fig. 2. XRD patterns of as-hydrothermally synthesized $CoSb_3$ powders (a); (*), ("), (^) and (+) symbols represent Sb, CoSb, $CoSb_2$ and $CoSb_3$ phases, respectively. XRD of annealed $CoSb_3$ powders at 585 °C for a duration of 5h inside an evacuated ampoule (b). The (*hkl*) Miller indices indicate cobalt skutterudite structure.

Fig. 3 illustrates the XRD patterns of $CoSb_3$-x$Cu_{0.6}Ni_{0.4}$ of all nanocomposite samples with x = 1, 3.5, 6, and 9 wt%. The major crystalline phase in all samples is $CoSb_3$; albeit, samples #1 to #4, fabricated by the first method, show higher purity. The impurity peaks are identified as $CoSb_2$, NiSb, and NiCoSb phases (labeled in Fig. 3). The intensity of impurity peaks is increased at higher concentrations of $Cu_{0.6}Ni_{0.4}$ nanoalloy, especially for the first set of samples. The impurity phases in the present composite samples could cause Ni deficiencies in the crystal structure of $Cu_{0.6}Ni_{0.4}$ (Fig. 3). No Cu_2O peak is detected in the XRD pattern of the $CoSb_3$-x$Cu_{0.6}Ni_{0.4}$ nanocomposites, indicating that $Cu_{0.6}Ni_{0.4}$ phase remains stable at the present fabrication conditions despite the formation of Ni deficiencies. The lattice parameter of all the $CoSb_3$-x$Cu_{0.6}Ni_{0.4}$ composites is refined with respect to the cell parameter of pure $CoSb_3$. The obtained results show the lattice parameter of the different samples varies between 9.031 Å and 9.037 Å (see

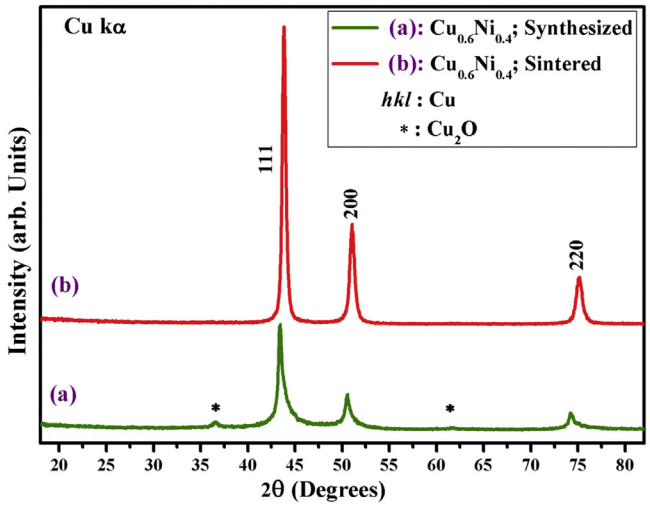

Fig. 1. XRD patterns of as-hydrothermally synthesized $Cu_{0.6}Ni_{0.4}$ powders (a); asterisk symbol (*) denotes Cu_2O phase. XRD of annealed $Cu_{0.6}Ni_{0.4}$ powders at 560 °C for a duration of 5h inside an evacuated ampoule (b). The (*hkl*) Miller indices represent that of the face-centered cubic copper structure, space group $Fm\bar{3}m$ (#225).

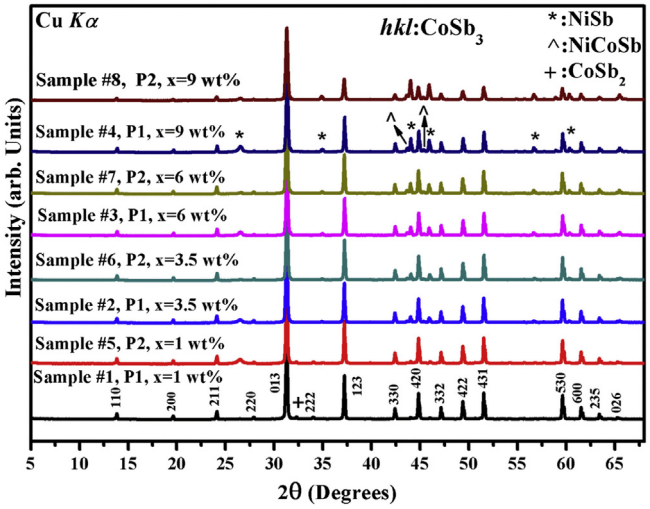

Fig. 3. XRD patterns of $CoSb_3$-x$Cu_{0.6}Ni_{0.4}$ nanocomposites with x = 1, 3.5, 6 and 9 wt% fabricated through P1 (samples #1 through #4) and P2 (samples #5 through #8). (*), (^) and (+) symbols represent traces of NiSb, NiCoSb, and $CoSb_2$ impurity phases, respectively. The (*hkl*) Miller indices indicate cobalt skutterudite structure.

supplementary), indicating that the host phase remains pure, as compared with other reports for pure cobalt skutterudite system [23,24,28,41,42].

The bulk density of the samples ranges between 63% and 73% of the theoretical density indicating a highly porous structure (Table 1). The relative bulk density of the samples fabricated through P1 is relatively lower than that of those samples fabricated through P2. The relative bulk density is reduced by the $Cu_{0.6}Ni_{0.4}$ nanoalloy ratio, especially for the second set of the samples.

The FE-SEM image of as-hydrothermally synthesized $Cu_{0.6}Ni_{0.4}$ powder is illustrated in Fig. 4. It shows the agglomeration of $Cu_{0.6}Ni_{0.4}$ nano-particles. The FE-SEM images of the fractured surfaces of $CoSb_3$-x$Cu_{0.6}Ni_{0.4}$ nanocomposites from samples #2 and #6 in Fig. 5a and b, respectively, show $CoSb_3$ grains with 300−600 nm in size (Fig. 5a), which co-exist with smaller size particles that appeared on the grains and interfaces of the larger $CoSb_3$ grains. These smaller particles that are pointed to with the red color arrow symbols might be $Cu_{0.6}Ni_{0.4}$. The $Cu_{0.6}Ni_{0.4}$ nanoinclusions range between 50 and 150 nm in size (Fig. 5a). According to the SEM micrographs, the size of $CoSb_3$ particles fabricated through P2 is comparatively larger than the size of $CoSb_3$ particles fabricated through P1 for the same amount of x. Moreover, the size of $CoSb_3$ particles fabricated through P1 is reduced with the increase in the content of $Cu_{0.6}Ni_{0.4}$ nanoalloy. In addition, Fig. 5 show that the first fabrication method (Fig. 5a) resulted in a more evenly embedded $Cu_{0.6}Ni_{0.4}$ nanoinclusions within the microstructure of the composite compared to the second fabrication method (Fig. 5b). This microstructure is promising for enhancing TE properties of $CoSb_3$. As Fig. 5b shows, $CoSb_3$-x$Cu_{0.6}Ni_{0.4}$ nanocomposites that were fabricated through P2 led aggregation of $Cu_{0.6}Ni_{0.4}$ particles on the grains of $CoSb_3$ crystals unevenly. The EDS analysis of a randomly selected area of sample #2 (Fig. 5c), together with a quantitative atomic percentage, are tabulated in Fig. 5d. The results confirm the presence of Co, Sb, Cu, and Ni element in the composites (Fig. 5d). The elemental maps for samples #2 and #6 (Fig. 5e and f) indicate a more uniform distribution of elements for sample #2, which was prepared through P1 process than that of sample #6 prepared through P2 fabrication process. Also, the SEM micrographs show that $CoSb_3$-x$Cu_{0.6}Ni_{0.4}$ nanocomposites are relatively porous, which is in agreement with their low relative bulk densities (Table 1).

2.2. Measurement of magnetic moment, charge carriers concentration and mobility

Fig. 6 displays the inverse magnetic moment of samples #1, 2, 3, and #4 as a function of temperature between 2 K and 400 K, under the applied auxiliary magnetic field of about 0.1 T. The magnetization of all samples is decreased with temperature and increased with the concentration of $Cu_{0.6}Ni_{0.4}$ phase. Magnetization data shown in Fig. 6 suggested that $CoSb_3$-x$Cu_{0.6}Ni_{0.4}$ samples are diamagnetic at around room temperature and has a weak Curie-

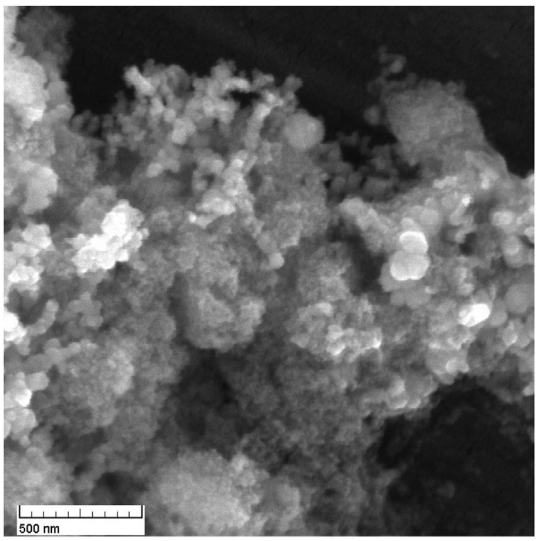

Fig. 4. FE-SEM image of as-hydrothermally synthesized powders of agglomerated $Cu_{0.6}Ni_{0.4}$ nanoparticles.

Weiss contribution at low temperature, which agrees with previous reports [48,49]. Diamagnetization is caused by the zero-spin electron configuration of Co^{3+}. With the increase in $Cu_{0.6}Ni_{0.4}$, an increase in magnetization might originate from the low spin configuration of Ni ions [48].

The Hall effect and mobility of $CoSb_3$-x$Cu_{0.6}Ni_{0.4}$ nanocomposites are measured at room temperature, and results are presented in Table 1. The Hall charge carrier concentrations are negative for all the samples, indicating electron as the majority charge carrier. The electron concentration is increased with the concentration of $Cu_{0.6}Ni_{0.4}$ nanoalloy in both sets of samples. The maximum electron concentrations of $n = 1 \times 10^{20} cm^{-3}$ and $8 \times 10^{20} cm^{-3}$ were obtained for samples #4 and #8, respectively. The significant difference in electron concentration between sample #4 and #8 might be due to uneven distribution of $Cu_{0.6}Ni_{0.4}$ nanoalloys in the $CoSb_3$ matrix of samples prepared by the second fabrication method (Fig. 5). The Hall mobility of electrons fluctuates between 15 and 5 $cm^2V^{-1}s^{-1}$ for all the samples (Table 1). The mobility remains less sensitive to the content of $Cu_{0.6}Ni_{0.4}$ nanoalloy for the first set of samples compared to the second set. This suggests that embedded $Cu_{0.6}Ni_{0.4}$ nanoparticles have an insignificant influence on the electron mobility reduction, presumably due to the formation of a dense structure of $CoSb_3$-x$Cu_{0.6}Ni_{0.4}$ composite. Hall data of sample #8 shows that electrons mobility correlates with the charge carrier concentration (Table 1). The relatively low electron mobility in conjunction with its relatively high carrier concentration of sample #8 might originate from the increased electron

Table 1
Physical properties obtained for $CoSb_3$-x$Cu_{0.6}Ni_{0.4}$ nanocomposite samples fabricated through procedures P1 and P2.

Physical Property / Samples	Relative Bulk Density (%)	Electron Concentration (10^{19} cm^{-3})	Mobility (cm^2/s.V)	E_b(meV) $312 \leq T/K < 605$	E_b (meV) $655 < T/K \leq 800$
Sample #1; P1; x = 1 wt%	65	1.9	15	36	156
Sample #2; P1; x = 3.5 wt%	63	2.8	15	33	135
Sample #3; P1; x = 6 wt%	63	5	14	30	125
Sample #4; P1; x = 9 wt%	65	10	11	24	102
Sample #5; P2; x = 1 wt%	73	2	13	41	234
Sample #6; P2; x = 3.5 wt%	68	2.7	14	35	155
Sample #7; P2; x = 6 wt%	66	4	10	33	138
Sample #8; P2; x = 9 wt%	66	80	5	11	51

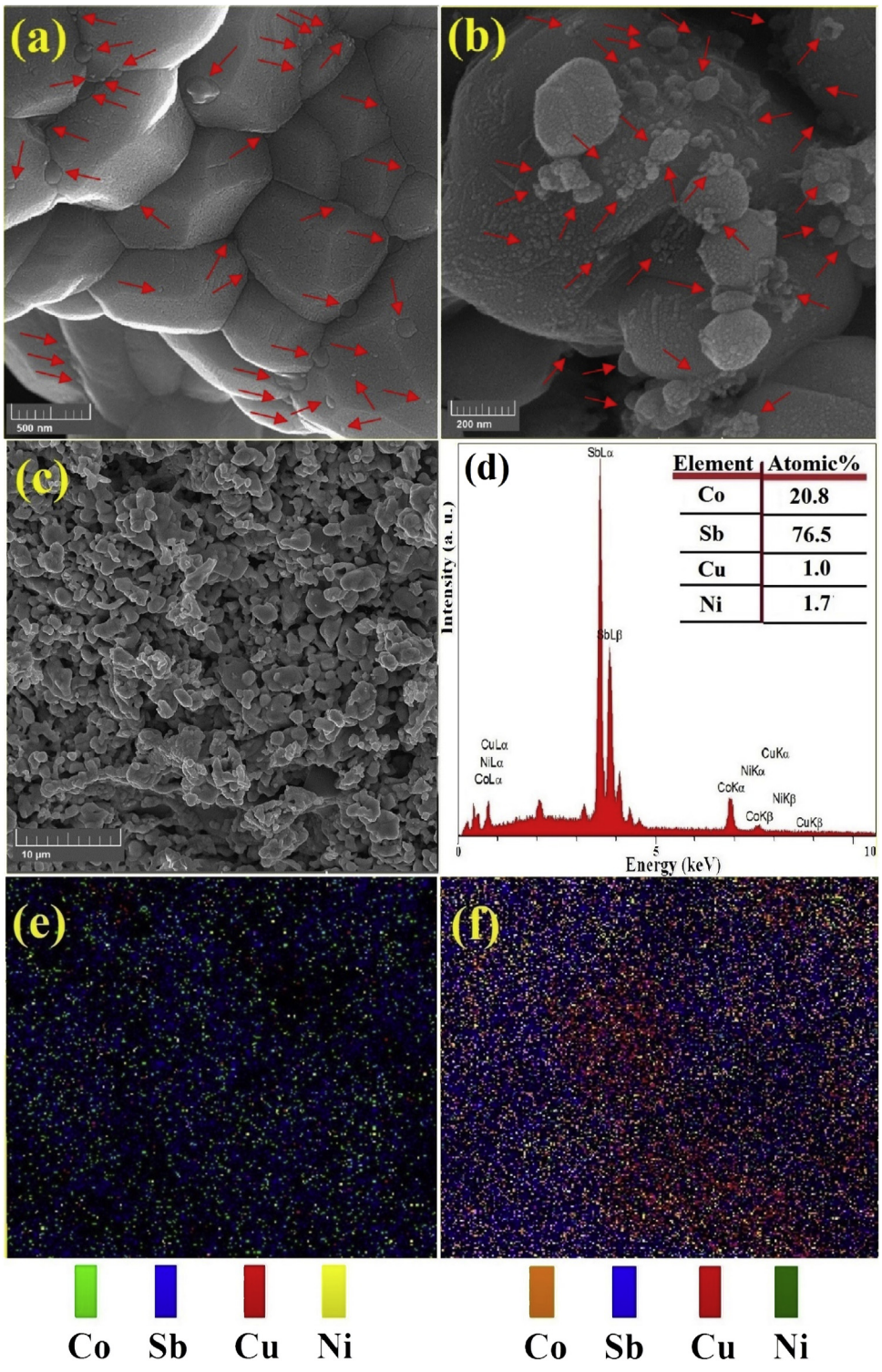

Fig. 5. FE-SEM images from the fractured surface of $CoSb_3$-x$Cu_{0.6}Ni_{0.4}$ nanocomposites representatively taken for samples #2 with x = 3.5 wt%, fabricated through P1 (a), and sample #6 with x = 3.5 wt%, fabricated through P2 (b); the quantitative EDX composition analysis (d) is randomly obtained from a selected area of sample #2 (c); the EDX elemental mapping representatively checked for samples #2 (e) and sample #6 (f).

scattering from those unevenly distributed electron pockets related to $Cu_{0.6}Ni_{0.4}$ nanoalloys and traces of other impurity phases (Fig. 3).

2.3. Measurement and analysis of thermoelectric properties

The electrical conductivity of $CoSb_3$-x$Cu_{0.6}Ni_{0.4}$ nanocomposites with x = 1, 3.5, 6 and 9 wt% is enhanced with $Cu_{0.6}Ni_{0.4}$ nanoalloy concentrations (Fig. 7). It is worth to mention that the electrical conductivity of hydrothermally synthesized $Cu_{0.6}Ni_{0.4}$ alloy displayed almost temperature-independent behavior from 300 K to 550 K with an average value of $7 \times 10^5\ \Omega^{-1}m^{-1}$ [43]. Compared with that of $CoSb_3$ material synthesized using the same

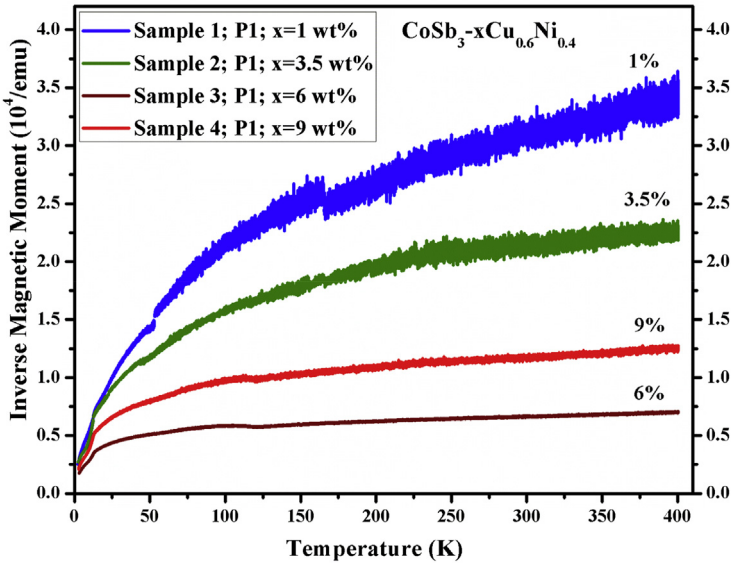

Fig. 6. Inverse magnetic susceptibility of $CoSb_3$-x$Cu_{0.6}Ni_{0.4}$ nanocomposites with x = 1, 3.5, 6, and 9 wt% (samples #1 through #4 fabricated using P1) as a function of temperature between 2 K and 400 K, under the applied auxiliary magnetic field of about 0.1 T.

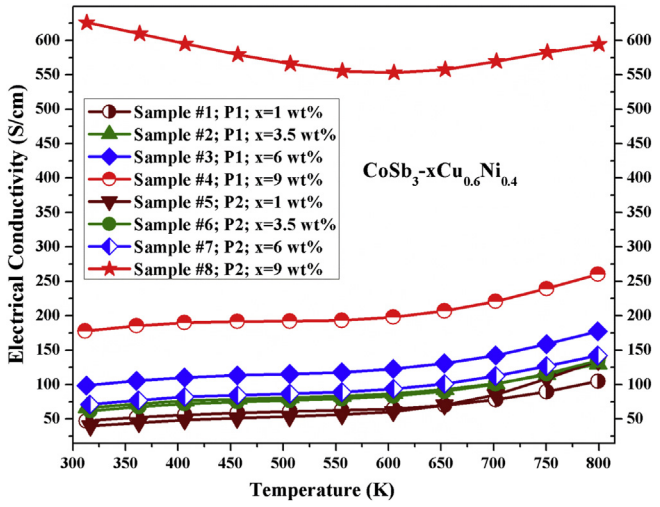

Fig. 7. The temperature dependence of electrical conductivity of $CoSb_3$-x$Cu_{0.6}Ni_{0.4}$ nanocomposites with x = 1, 3.5, 6, and 9 wt% between 312 K and 800 K; samples #1 through #4 were fabricated using P1 and samples #5 through #8 were fabricated using P2.

hydrothermal procedure and possessing comparable bulk density [39], the least enlargement of the electrical conductivity of the present composites is over four-times. All the electrical conductivity curves similarly display nonmetallic temperature dependence between room temperature and 800 K, except sample #8. The temperature dependence of the electrical conductivity of sample #8 decreases with increasing temperature below 600 K, resembles metallic behavior, and it switches to nonmetallic behavior for $600 < T/K \leq 800$. Commonly, the electrical conductivity of semiconductor materials such as pristine $CoSb_3$ displays strong temperature dependence. However, the relatively weak temperature dependence of the electrical conductivity of $CoSb_3$-x$Cu_{0.6}Ni_{0.4}$ nanocomposites might arise from the high porosity of samples. Similar weak temperature dependence of electrical conductivity was also reported for $CoSb_3$ samples fabricated using melting quenching-annealing-plasma activated sintering and hydrothermal synthesis followed by annealing procedures [21,39]. The relatively low electrical conductivity values of samples might be due to high porosity in conjunction with a high concentration of grain boundaries, which features nanostructures. Highly porous structures could trap charge carriers, and a high concentration of grain boundaries could expedite scattering of charge carriers. Single-phase $CoSb_3$ samples fabricated via similar hydrothermal procedure showed a relatively low electrical conductivity as well [39,42]. For both sets of samples, the electrical conductivity is increased with the content of $Cu_{0.6}Ni_{0.4}$ nanoalloys. As seen on the micrograph images (Figs. 4 and 5), nanosized $Cu_{0.6}Ni_{0.4}$ particles connect $CoSb_3$ grains to its nearest neighbors; these highly conductive particles increase the electrical conductivity of the composite. The samples with x = 1 and 3.5 wt% showed almost the same electrical conductivity values, over the temperature range for both fabrication methods (Fig. 7). The electrical conductivity of samples with x = 6 wt% show similar behavior over the whole temperature range; however, the sample fabricated by the first method has slightly higher electrical conductivity values, mainly due to its higher electron mobility (Table 1). The significantly enhanced electrical conductivity of sample #8 might be attributed to its 10-times larger carrier concentration, compared to that of sample #4 and the rest of the samples. The relatively high carrier concentration and hence the significantly increased electrical conductivity of sample #8 could arise from a kind of short-range percolation as a result of inhomogeneous distribution of $Cu_{0.6}Ni_{0.4}$ within $CoSb_3$ matrix.

The secondary phase of $Cu_{0.6}Ni_{0.4}$ nanoalloy could tune interfacial energy barriers to facilitate electron transition within grain boundaries. The influence of a second phase on the electron transport at grain boundaries of the matrix material can be studied by applying a potential barrier model [50,51]. The electrical conductivity correlates to the height of the potential energy barrier through Eq. (2):

$$\sigma \propto T^{-0.5} e^{-\frac{E_b}{k_B T}} \tag{2}$$

Where σ is electrical conductivity at temperature T; E_b and k_B are the height of potential energy barrier and the Boltzmann constant, respectively. Fig. 8 shows the results of fitting the electrical

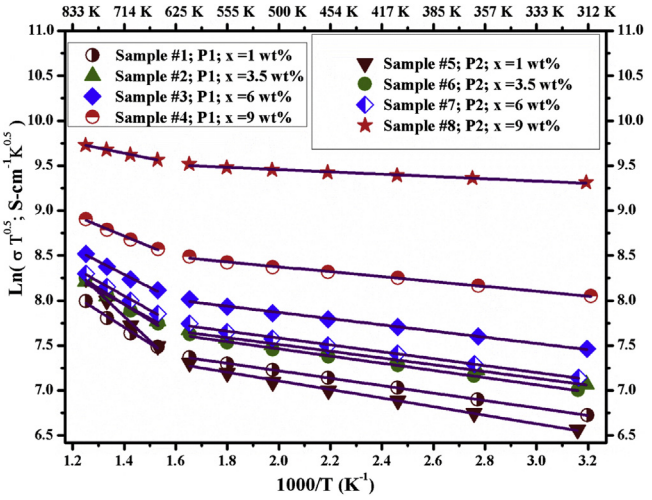

Fig. 8. Linear fitting of $Ln(\sigma T^{0.5})$ versus T^{-1} for $CoSb_3$-$xCu_{0.6}Ni_{0.4}$ nanocomposites within two temperature regions of $312 \leq T/K < 605$ and $655 < T/K \leq 800$. The slopes of fitted curves are used to estimate the height of the grain boundary potential barrier (E_b); samples #1 through #4 were fabricated using P1, and samples #5 through #8 were fabricated using P2.

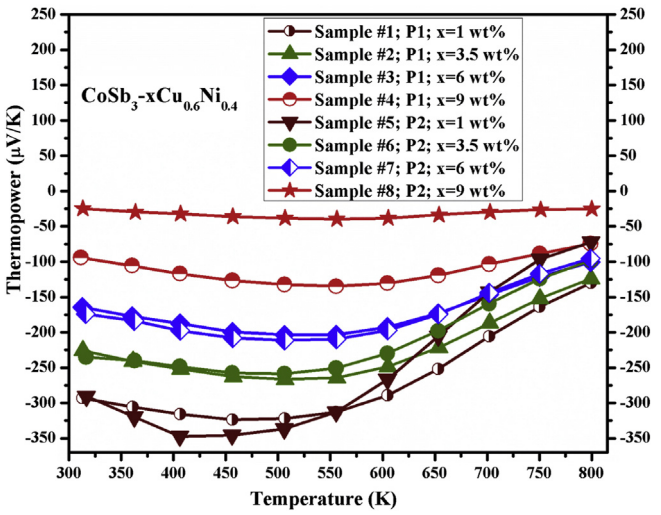

Fig. 10. The temperature dependence of thermopower of $CoSb_3$-$xCu_{0.6}Ni_{0.4}$ nanocomposites with x = 1, 3.5, 6, and 9 wt% between 312 K and 800 K; samples #1 through #4 were fabricated using P1 and samples #5 through #8 were fabricated using P2.

conductivity curves with Eq. (2). For each curve, the appropriate fitting is obtained within temperature intervals of $312 \leq T/K < 605$ and $655 < T/K \leq 800$. The estimated E_b values obtained at both temperature regions are presented in Table 1. The lower temperature region corresponds to smaller E_b values (Fig. 8), while the higher temperature region corresponds to larger E_b values (Table 1). At both temperature ranges, E_b is reduced systematically with the concentration of $Cu_{0.6}Ni_{0.4}$ nanoalloy for both sets of samples. The estimated E_b values using Eq. (2) for the second set of samples are slightly larger than that of the first set, except sample #8. At lower temperature range, the highest E_b value is 41 meV, and the lowest E_b value is 11 meV, respectively for sample #5 and #8. E_b is increased at $655 < T/K \leq 800$ region and its magnitudes vary between 234 meV and 51 meV for sample #5 and 8, respectively (Table 1). The significantly increased E_b values at $655 < T/K \leq 800$ might be due to the height of the potential barrier that holes carriers encounter during transition through grain boundaries. In other words, the selectively filtering of the lower energy holes carriers via the grain boundary could have correlated with the increased height of the potential barrier at higher temperature regions. The mentioned mechanism is schematically described in Fig. 9, thereat, the minority impurity states at a lower temperature (part 1) is declined the barrier height that electrons encounter, while at the higher temperature region (part 2) the depletion of impurity states in conjunction with contribution of holes carriers from valence band is increased the height of the potential barrier (E_b). The depletion of impurity electronic states with increasing temperature would lead to the activation of intrinsic states at higher temperature regions. This mechanism would emerge the bipolar effect in $CoSb_3$ structure thereat both electron and holes would contribute to transport properties [29,52,53]. The obtained data from fitted curves to the electrical conductivity values using Eq. (2) show that the estimated values of E_b is reduced at $655 < T/K \leq 800$ with the concentration of $Cu_{0.6}Ni_{0.4}$ nanoalloys. The direct contribution of $Cu_{0.6}Ni_{0.4}$ electron states to the transport properties of $CoSb_3$ system could have presumably led to the mentioned mechanism.

The thermopowers of the $CoSb_3$-$xCu_{0.6}Ni_{0.4}$ nanocomposites (Fig. 10) are negative, demonstrating n-type semiconductors. The room temperature absolute thermopower values of samples are reduced systematically with increasing the content of $Cu_{0.6}Ni_{0.4}$ nanoalloy (Fig. 10). The largest absolute thermopower value was obtained for composite samples with x = 1 wt%, and the lowest value corresponds to the sample #8. On the other hand, nanocomposites having the same content of x = 3.5 and 6 wt% display almost the same thermopower values below 525 K. The thermopower of sample #8 varies slightly at 25–40 μV/K over the measured temperature range. The thermopower values as a function of electron concentration for sample #8 resembles the metallic behavior where thermopower is a function of electron concentration $(n)^{-\frac{2}{3}}$. Compared with that of $CoSb_3$ material synthesized using the same hydrothermal procedure [39], the absolute thermopower value of present $CoSb_3$-$xCu_{0.6}Ni_{0.4}$ nanocomposites is enhanced up to about 20% for the sample with x = 1 wt% (Fig. 10).

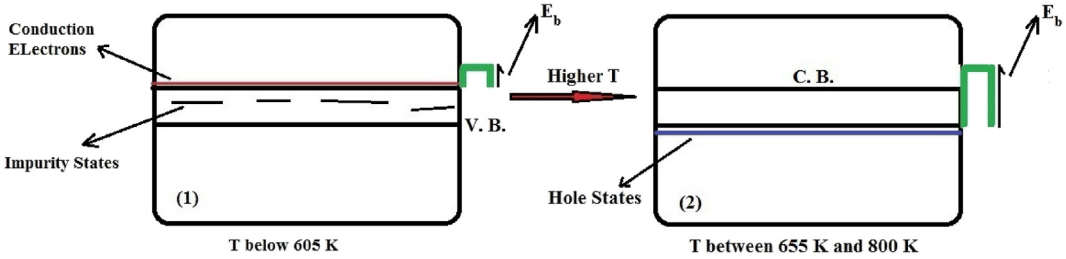

Fig. 9. A schematic to explain the influence of holes carriers to the enlarged E_b values at $655 < T/K \leq 800$ temperature region as compared with that of the contribution of impurity states to the electronic properties below 605 K.

Furthermore, the reduction of thermopower due to the bipolar effect that is discussed in the following discussion is partially suppressed, and the slope of its curve as a function of temperature is decreased as a result of compositing with $Cu_{0.6}Ni_{0.4}$ nanoalloy.

Considering a partial contribution of $Cu_{0.6}Ni_{0.4}$ and in situ formation of the impurity phase, the total thermopower of $CoSb_3$-$xCu_{0.6}Ni_{0.4}$ nanocomposites could be expressed using Eq. (3),

$$S = \sum_i \frac{\sigma_i S_i}{\sigma} = \frac{\sigma_m S_m + \sigma_a S_a + \sigma_{ip} S_{ip}}{\sigma_m + \sigma_a + \sigma_{ip}} \quad (3)$$

where S, S_i, σ_i and $\sigma = \sigma_m + \sigma_a + \sigma_{ip}$ denote total thermopower, partial thermopower, partial electrical conductivity, and total electrical conductivity, respectively. In Eq. (3), *m*, *a* and *ip* indices represent $CoSb_3$ matrix, $Cu_{0.6}Ni_{0.4}$ nanoalloy, and in situ formed impurity phases, respectively. The thermopower of hydrothermally synthesized $CoSb_3$ is usually negative below 400 K [39,41]. The absolute thermopower of n-type $Cu_{0.6}Ni_{0.4}$ alloy was shown to increase with temperature from about −44 μV/K at 300 K to about −62 μV/K at 550 K [43]. The relatively reduced room temperature thermopower of the composites might arise from an increased $\frac{\sigma_i}{\sigma}$ ratio at a higher concentration of $Cu_{0.6}Ni_{0.4}$ and impurity phases. The reduced values of *S* with $Cu_{0.6}Ni_{0.4}$ concentration imply that impurity traces presumably could have been p-type semiconductors (Fig. 3); hence it could have led to further reduction of thermopower at room temperature (Fig. 10). Above 400 K, the probable contribution of the thermally activated intrinsic holes carriers from $CoSb_3$ matrix has compensated the corresponding thermopower component (S_m) due to the bipolar effect [29,39,41].

It is commonly known that the bipolar effect mainly arises from the intrinsic band structure of the materials and hence can affect thermoelectric transport properties, including electrical conductivity, thermal conductivity, and thermopower. Typically, the bipolar effect reduces the thermopower but enhances both thermal conductivity and electrical conductivity. All nanocomposite samples (Fig. 10) show the bipolar effect. However, the temperature corresponds to the maximum thermopower is increased with the concentration of $Cu_{0.6}Ni_{0.4}$.

Fig. 11 displays the thermoelectric power factor of $CoSb_3$-$xCu_{0.6}Ni_{0.4}$ with x = 1, 3.5, 6, and 9 wt% between room temperature and 800 K. The maximum power factor of about 6.33 μWcm^{-1}K^{-2} is obtained for sample #1 around 506 K, slightly improved compared to the previous reports for pristine $CoSb_3$ [24,29,41,52]. The peak of power factor is shifted to higher temperatures, while the values are reduced with the ratio of $Cu_{0.6}Ni_{0.4}$ nanoalloys, mainly due to the significant reduction of the total thermopower (Fig. 10).

The total thermal conductivities of $CoSb_3$-$xCu_{0.6}Ni_{0.4}$ nanocomposites between 312 K and 800 K are illustrated in Fig. 12.

Microstructural analysis (Fig. 5) indicated that the size of the skutterudite grains is larger than the calculated phonon mean-free-path (135 nm) for $CoSb_3$ structure and therefore larger than the value predicted by kinetic theory ($\sim 4nm$). Also, considering the fact that the transport properties measurement is performed well above 50 K, the special phonon confinement effects on the specific heat capacity of the composites are negligible [54,55]. Hence, by assuming grain size-independent specific heat capacity, we may consider a constant C_{pi} for each component and apply Eq. (1) to estimate C_p of the samples. The largest total thermal conductivity values are obtained for sample #8, and the smallest values were obtained for sample #1 (Fig. 12). For the first set of samples, κ values are significantly lower than that of the second set, except for the samples #3 and #7 (x = 6 wt%). The κ of all samples is decreased with temperature for $312 \leq T/K \leq 600$, albeit at different rates; for $600 < T(K) \leq 800$, κ is increased with temperature for all samples except sample #8 that κ almost plateau remains roughly constant above 555 K. This is due to the large carrier concentration of this sample (Table 1). Compared with that of $CoSb_3$ material synthesized using the same hydrothermal procedure [39], the measured total thermal conductivity of present $CoSb_3$-$xCu_{0.6}Ni_{0.4}$ nanocomposites is enlarged over two-times and increased upon increasing the content of $Cu_{0.6}Ni_{0.4}$ within the same temperature interval. The measured total thermal conductivity of $Cu_{0.6}Ni_{0.4}$ alloy showed a relatively small increase with temperature from about 3 Wm^{-1}K^{-1} at 300 K to about 3.5 Wm^{-1}K^{-1} at 550 K [43].

The lattice phonon component of the total thermal conductivity could be estimated by subtracting the electronic contribution from the overall thermal conductivity $\kappa_L = \kappa - \kappa_e - \kappa_{bi}$. In the absence of the bipolar effect κ_{bi}, the electronic contribution (κ_e) to the thermal conductivity could be estimated using the Wiedemann-Franz law, $\kappa_e = \sigma LT$; thereat $L = \frac{\pi^2}{3}(\frac{k_B}{e})^2 \cong 2.45 \times 10^{-8}\ W\Omega K^{-2}$ (for metals or

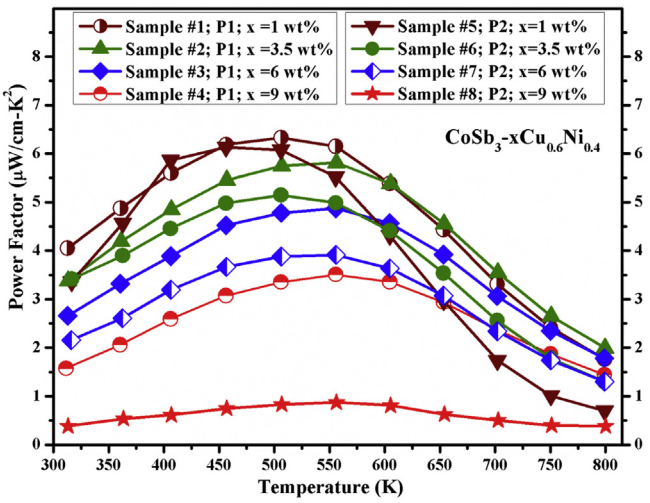

Fig. 11. The thermoelectric power factor of $CoSb_3$-$xCu_{0.6}Ni_{0.4}$ nanocomposites with x = 1, 3.5, 6, and 9 wt% as a function of temperature between 312 K and 800 K; samples #1 through #4 were fabricated using P1 and samples #5 through #8 were fabricated using P2.

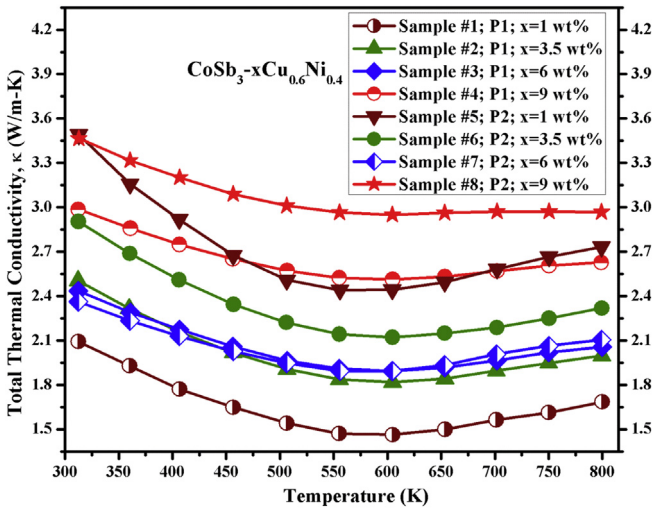

Fig. 12. The total thermal conductivity (κ) of $CoSb_3$-$xCu_{0.6}Ni_{0.4}$ nanocomposites with x = 1, 3.5, 6, and 9 wt% as a function of temperature between 312 K and 800 K; samples #1 through #4 were fabricated using P1 and samples #5 through #8 were fabricated using P2.

degenerate semiconductors), where L is the Lorenz number, and σ is the electrical conductivity at absolute temperature T. The contribution of σLT is estimated, and the obtained results show the corresponding magnitudes varies from 0.036 $Wm^{-1}K^{-1}$ to 0.51 $Wm^{-1}K^{-1}$ for $312 \leq T/K \leq 800$ for all the samples, except sample #8 (x = 9 wt%). The magnitudes of σLT for sample #8 varies from 0.48 $Wm^{-1}K^{-1}$ to 1.16 $Wm^{-1}K^{-1}$ for $312 \leq T/K \leq 800$, which is in agreement with the corresponding relatively high electrical conductivity of the title composite (Fig. 7). By disregarding the deviation of L for composite samples from that of a single-phase metal or degenerate semiconductor, and in the presence of the bipolar effect κ_{bi}, the electronic contribution to the total thermal conductivity could be estimated by $\sigma LT + \kappa_{bi}$; in which the bipolar contribution κ_{bi} could be estimated using Eq. (4) [53].

$$\kappa_{bi} = \frac{\sigma_e \sigma_h}{\sigma_e + \sigma_h}(S_e - S_h)^2 T \quad (4)$$

where, $\sigma_{e,h}$ and $S_{e,h}$ represents electrons (holes) contribution to the electrical conductivity and thermopower, respectively.

The temperature dependence of $\kappa - \sigma LT$ for all samples is represented in Fig. 13. All samples present a bipolar effect curvature except for sample #8, which has much higher charge carrier concentration.

The onset temperature for bipolar effect can be estimated by observing the bipolar trends shown by the transport properties. In this work, the onset temperature of the bipolar effect for each sample is compared with respect to their corresponding thermal conductivity κ. The relatively small magnitudes of σLT (less than 17% of the total κ) could be attributed to the relatively weak electrical conductivity of the present $CoSb_3$-x$Cu_{0.6}Ni_{0.4}$ composites. Fig. 13 shows the sum of the lattice and bipolar thermal conductivity, i.e., $\kappa - \sigma LT = \kappa_L + \kappa_{bi}$. κ_L generally has a reducing trend with temperature due to the increase of the 3-phonon scattering. But κ_{bi} slope versus temperature is positive due to the increase in the population of the thermally excited carriers. As such, at low temperatures, lattice contribution is dominant, and at high temperatures, the bipolar contribution controls the trend of $\kappa -$ σLT. It can be seen that for all samples, except sample 5, the curvature changes at approximately 550–600 K. The same trend is observed for the thermopower versus temperature (Fig. 10). The exact onset temperature of seeing the bipolar effect may be somewhat different for the thermal conductivity and the thermopower depending on the relative strength of their various components. Sample 5 shows a smaller κ_{bi} onset temperature for both the thermal conductivity and thermopower, which is attributed to its smaller carrier concentration.

Fig. 14 displays the dimensionless TE figure of merit (zT) for $CoSb_3$-x$Cu_{0.6}Ni_{0.4}$nanocomposites with x = 1, 3.5, 6, and 9 wt% between room temperature and 800 K. The maximum zT of about 0.23 is achieved at 555 K for sample #1. In general, the first set of samples show higher zT values than the second set (for the same amount of $Cu_{0.6}Ni_{0.4}$ nanoalloy). The obtained zT value of 0.23 is higher than that of unfilled pristine $CoSb_3$ synthesized using the hydrothermal procedure, or previous reports used other fabrication methods [19,36,37,39,41]. Hence, the fabrication of potential TE composites using the first procedure (P1) in conjunction with the appropriate choice of nanoinclusions seems a promising route to enhance zT of corresponding materials beyond its current values.

3. Conclusion

$CoSb_3$ and $Cu_{0.6}Ni_{0.4}$ nanoalloy were separately synthesized through hydrothermal procedures. The influence of fabrication sequences of composite materials on the formation of the desired crystal phase and transport properties of the final composite materials was studied. The obtained samples were highly porous in nature, and traces of impurity phases, including $CoSb_2$, NiSb, and NiCoSb were identified in the final compounds.

Nanoinclusions vary in size between 50 nm and 150 nm, while $CoSb_3$ particles are between 300 nm and 600 nm. The EDX mapping shows a more uniform distribution of $Cu_{0.6}Ni_{0.4}$ nanoalloy in the first set of samples.

The magnetization of the first set of samples increased with the concentration of $Cu_{0.6}Ni_{0.4}$ nanoalloys, while it is decreased with temperature. The electrical conductivity of $CoSb_3$-x$Cu_{0.6}Ni_{0.4}$ nanocomposites is enhanced with the content of $Cu_{0.6}Ni_{0.4}$. The electrical conductivity demonstrates weak temperature dependence, probably due to the relatively high porosity of the samples. The electrical conductivity of all samples displays nonmetallic temperature dependence behavior, except sample with x = 9 wt%, which has much higher carrier concentration than the other samples. The obtained results from the applied potential barrier model

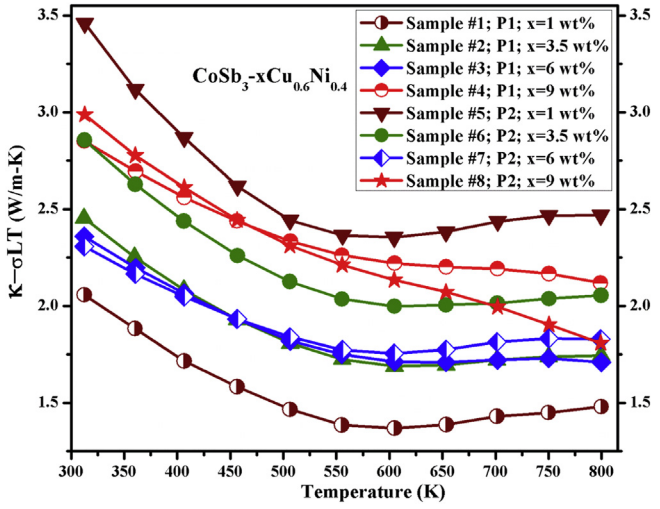

Fig. 13. The temperature dependence of $\kappa - \sigma LT$ calculated for $CoSb_3$-x$Cu_{0.6}Ni_{0.4}$ nanocomposites with x = 1, 3.5, 6 and 9 wt% between 312 K and 800 K thereat the σLT term was estimated using the Wiedemann-Franz law.

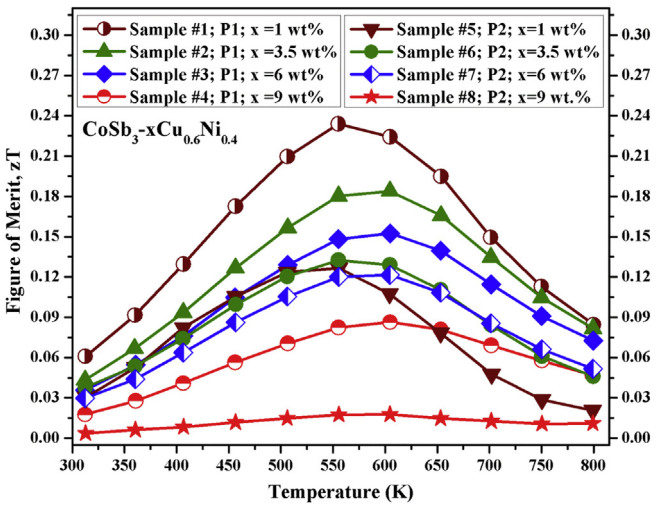

Fig. 14. The zT as a function of temperature for $CoSb_3$-x$Cu_{0.6}Ni_{0.4}$ nanocomposites with x = 1, 3.5, 6, and 9 wt% between 312 K and 800 K; samples #1 through #4 were fabricated using P1 and samples #5 through #8 were fabricated using P2.

showed that the height of the energy barrier was reduced with increasing content of $Cu_{0.6}Ni_{0.4}$ nanoinclusions for both sets of samples.

The temperature-dependent thermopower values displayed that the onset of bipolar effect is shifted to higher temperatures with the concentration of $Cu_{0.6}Ni_{0.4}$.

The first set of samples possesses lower total thermal conductivity than the samples fabricated by a second fabrication method, presumably due to their relatively high porosity. On the other hand, the higher carrier concentration of sample #8 is an exception that displays a high contribution of the electronic component to its total thermal conductivity.

The maximum zT value was obtained at 555 K for the sample with x = 1 wt%, fabricated by the first method. The zT of present $CoSb_3$-x$Cu_{0.6}Ni_{0.4}$ is higher than pristine $CoSb_3$, synthesized by the same hydrothermal method. In general, the zT values of samples fabricated by the first method are larger than those made by the second method for samples with the same amount of $Cu_{0.6}Ni_{0.4}$ nanoalloys.

CRediT authorship contribution statement

Ahmad Gharleghi: Conceptualization, Formal analysis, Investigation, Methodology, Supervision, Resources, Writing - original draft, Writing - review & editing. **Md Mobarak Hossain Polash:** Formal analysis. **Rasoul Malekfar:** Funding acquisition. **Sima Aminorroaya Yamini:** Writing - review & editing. **Daryoosh Vashaee:** Funding acquisition, Investigation, Supervision, Resources, Writing - review & editing.

Declaration of competing interest

There is no conflict of interest to declare.

Acknowledgments

This work was partially supported by the National Science Foundation, United States under grant numbers ECCS-1351533, ECCS-1515005, and ECCS-1711253. AG acknowledges the supports from I. R. Iran's National Elite Foundation-3321.

Appendix A. Supplementary data

Supplementary data to this article can be found online at https://doi.org/10.1016/j.jallcom.2020.156188.

References

[1] D. Beretta, N. Neophytou, J.M. Hodges, M.G. Kanatzidis, D. Narducci, M. Martin-Gonzalez, M. Beekman, B. Balke, G. Cerretti, W. Tremel, Thermoelectrics: from history, a window to the future, Mater. Sci. Eng.: R: Rep. (2018) 3–18.
[2] R.A. Kishore, A. Nozariasbmarz, B. Poudel, M. Sanghadasa, S. Priya, Ultra-high performance wearable thermoelectric coolers with less materials, Nat. Commun. 10 (2019) 1765.
[3] Y. Wang, L. Yang, X.L. Shi, X. Shi, L. Chen, M.S. Dargusch, J. Zou, Z.G. Chen, Flexible thermoelectric materials and generators: challenges and innovations, Adv. Mater. (2019) 1807916.
[4] G.S. Nolas, J. Sharp, J. Goldsmid, Thermoelectrics: basic principles and new materials developments, Springer Verlag, Berlin/ Heidelberg, Germany, 2001. Page 99.
[5] X. Qian, H. Wu, D. Wang, Y. Zhang, J. Wang, G. Wang, L. Zheng, S.J. Pennycook, L.-D. Zhao, Synergistically optimizing interdependent thermoelectric parameters of n-type PbSe through alloying CdSe, Energy Environ. Sci. 12 (2019) 1969–1978.
[6] Z.Z. Luo, X. Zhang, X. Hua, G. Tan, T.P. Bailey, J. Xu, C. Uher, C. Wolverton, V.P. Dravid, Q. Yan, High thermoelectric performance in supersaturated solid solutions and nanostructured n-type PbTe–GeTe, Adv. Funct. Mater. 28 (2018) 1801617.
[7] J. Schaumann, M. Loor, D. Ünal, A. Mudring, S. Heimann, U. Hagemann, S. Schulz, F. Maculewicz, G. Schierning, Improving the zT value of thermoelectrics by nanostructuring: tuning the nanoparticle morphology of Sb 2 Te 3 by using ionic liquids, Dalton Trans. 46 (2017) 656–668.
[8] G. Rogl, J. Bursik, A. Grytsiv, S. Puchegger, V. Soprunyuk, W. Schranz, X. Yan, E. Bauer, P. Rogl, Nanostructuring as a tool to adjust thermal expansion in high ZT skutterudites, Acta Mater. 145 (2018) 359–368.
[9] W. Yao, D. Yang, Y. Yan, K. Peng, H. Zhan, A. Liu, X. Lu, G. Wang, X. Zhou, Synergistic strategy to enhance the thermoelectric properties of CoSbS1−x Se x compounds via solid solution, ACS Appl. Mater. Interfaces 9 (2017) 10595–10601.
[10] S.H. Zaferani, R. Ghomashchi, D. Vashaee, Strategies for engineering phonon transport in Heusler thermoelectric compounds, Renew. Sustain. Energy Rev. 112 (2019) 158–169.
[11] Y. Suzuki, H. Nakamura, A supercell approach to the doping effect on the thermoelectric properties of SnSe, Phys. Chem. Chem. Phys. 17 (2015) 29647–29654.
[12] F. Fahrnbauer, S. Maier, M. Grundei, N. Giesbrecht, M. Nentwig, T. Rosenthal, G. Wagner, G.J. Snyder, O. Oeckler, Heterostructures of skutterudites and germanium antimony tellurides–structure analysis and thermoelectric properties of bulk samples, J. Mater. Chem. C 3 (2015) 10525–10533.
[13] K. Wei, J.N. Neu, Y. Lai, K.-W. Chen, D. Hobbis, G.S. Nolas, D.E. Graf, T. Siegrist, R.E. Baumbach, Enhanced thermoelectric performance of heavy-fermion compounds YbTM2Zn20 (TM= Co, Rh, Ir) at low temperatures, Science advances 5 (2019), eaaw6183.
[14] J. Zide, J.-H. Bahk, R. Singh, M. Zebarjadi, G. Zeng, H. Lu, J. Feser, D. Xu, S. Singer, Z. Bian, A. Majumdar, J. Bowers, A. Shakouri, A. Gossard, High efficiency semimetal/semiconductor nanocomposite thermoelectric materials, J. Appl. Phys. 108 (2010) 123702.
[15] C. Dun, C.A. Hewitt, H. Huang, J. Xu, C. Zhou, W. Huang, Y. Cui, W. Zhou, Q. Jiang, D.L. Carroll, Flexible n-type thermoelectric films based on Cu-doped Bi2Se3 nanoplate and Polyvinylidene Fluoride composite with decoupled Seebeck coefficient and electrical conductivity, Nano Energy 18 (2015) 306–314.
[16] C. Kim, J.Y. Baek, D.H. Lopez, D.H. Kim, H. Kim, Decoupling effect of electrical and thermal properties of Bi2Te3-polypyrrole hybrid material causing remarkable enhancement in thermoelectric performance, J. Ind. Eng. Chem. 71 (2019) 119–126.
[17] J.R. Durán Retamal, C.F. Kang, D.H. Lien, W.C. Kuo, Z.Y. Juang, M.L. Tsai, C.H. Ho, J.Y. Juang, V.K. Hsiao, Y.H. Chu, L.-J.L. Li, Y. Wu, J.-H. He, A nanostructuring method to decouple electrical and thermal transport through the formation of electrically triggered conductive nanofilaments, Adv. Mater. 30 (2018) 1705385.
[18] D. Park, H. Ju, T. Oh, J. Kim, Facile fabrication of one-dimensional Te/Cu 2 Te nanorod composites with improved thermoelectric power factor and low thermal conductivity, Sci. Rep. 8 (2018) 18082.
[19] A. Moure, M. Rull-Bravo, B. Abad, A. Del Campo, M.M. Rojo, M. Aguirre, A. Jacquot, J. Fernandez, M. Martin-Gonzalez, Thermoelectric Skutterudite/oxide nanocomposites: Effective decoupling of electrical and thermal conductivity by functional interfaces, Nano energy 31 (2017) 393–402.
[20] Z. Tu, X. Sun, X. Li, R. Li, L. Xi, J. Yang, Thermoelectric transport properties of Ni-, Pd-, and Pt-doped skutterudites with S-filling as charge compensation, AIP Adv. 9 (2019), 045325.
[21] T. Liang, X. Su, Y. Yan, G. Zheng, X. She, Y. You, C. Uher, M.G. Kanatzidis, X. Tang, Panoscopic approach for high-performance Te-doped skutterudite, NPG Asia Mater. 9 (2017) e352.
[22] V. Trivedi, M. Battabyal, P. Balasubramanian, G.M. Muralikrishna, P.K. Jain, R. Gopalan, Microstructure and doping effect on the enhancement of the thermoelectric properties of Ni doped Dy filled CoSb 3 skutterudites, Sustainable Energy & Fuels 2 (2018) 2687–2697.
[23] A. Gharleghi, Y.-H. Chu, F.-H. Lin, Z.-R. Yang, Y.-H. Pai, C.-J. Liu, Optimization and analysis of thermoelectric properties of unfilled Co1−x−y Ni x Fe y Sb3 synthesized via a rapid hydrothermal procedure, ACS Appl. Mater. Interfaces 8 (2016) 5205–5215.
[24] Y. Lei, W. Gao, R. Zheng, Y. Li, W. Chen, L. Zhang, R. Wan, H. Zhou, Z. Liu, P.K. Chu, Ultra-fast synthesis of Te-doped CoSb3 with excellent thermoelectric properties, ACS Appl. Energy Mater. 2 (2019) 4477–4485.
[25] P. Sun, B. Wei, J. Zhang, J.M. Tomczak, A. Strydom, M. Søndergaard, B.B. Iversen, F. Steglich, Large Seebeck effect by charge-mobility engineering, Nat. Commun. 6 (2015) 7475.
[26] J. Li, B. Duan, H. Yang, H. Wang, G. Li, J. Yang, G. Chen, P. Zhai, Thermoelectric properties of electronegatively filled SyCo4-xNixSb12 skutterudites, J. Mater. Chem. C 7 (2019) 8079–8085.
[27] X. Shi, J. Yang, J.R. Salvador, M. Chi, J.Y. Cho, H. Wang, S. Bai, J. Yang, W. Zhang, L. Chen, Multiple-filled skutterudites: high thermoelectric figure of merit through separately optimizing electrical and thermal transports, J. Am. Chem. Soc. 133 (2011) 7837–7846.
[28] S. Le Tonquesse, É. Alleno, V. Demange, V. Dorcet, L. Joanny, C. Prestipino, O. Rouleau, M. Pasturel, Innovative synthesis of mesostructured CoSb3-based skutterudites by magnesioreduction, J. Alloys Compd. 796 (2019) 176–184.
[29] W.-S. Liu, B.-P. Zhang, J.-F. Li, H.-L. Zhang, L.-D. Zhao, Enhanced thermoelectric properties in CoSb 3-x Te x alloys prepared by mechanical alloying and spark plasma sintering, J. Appl. Phys. 102 (2007) 103717.
[30] Y. Zhu, H. Shen, H. Chen, Effects of nano-TiO 2 dispersion on thermoelectric properties of Co 4 Sb 11.7 Te 0.3 composites, Rare Met. 31 (2012) 43–47.
[31] H. Li, X. Tang, Q. Zhang, C. Uher, High performance in x Ce y Co 4 Sb 12

thermoelectric materials with in situ forming nanostructured InSb phase, Appl. Phys. Lett. 94 (2009) 102114.
[32] X. Zhao, X. Shi, L. Chen, W. Zhang, S. Bai, Y. Pei, X. Li, T. Goto, Synthesis of Yb y Co 4 Sb 12/ Yb 2 O 3 composites and their thermoelectric properties, Appl. Phys. Lett. 89 (2006), 092121.
[33] Z. Xiong, X. Chen, X. Zhao, S. Bai, X. Huang, L. Chen, Effects of nano-TiO2 dispersion on the thermoelectric properties offilled-skutterudite Ba0. 22Co4Sb12, Solid State Sci. 11 (2009) 1612–1616.
[34] J. Mi, X. Zhao, T. Zhu, J. Tu, Thermoelectric properties of Yb0. 15Co4Sb12 based nanocomposites with CoSb3 nano-inclusion, J. Phys. Appl. Phys. 41 (2008) 205403.
[35] P. Alboni, X. Ji, J. He, N. Gothard, T.M. Tritt, Thermoelectric properties of La 0.9 $CoFe_3 Sb_{12}$–$CoSb_3$ skutterudite nanocomposites, J. Appl. Phys. 103 (2008) 113707.
[36] S. Yadav, S. Chaudhary, D.K. Pandya, Incorporation of MoS_2 nanosheets in $CoSb_3$ matrix as an efficient novel strategy to enhance its thermoelectric performance, Appl. Surf. Sci. 435 (2018) 1265–1272.
[37] H. Zhu, S. Liang, T. Ouyang, S. Yue, J. Jiang, Thermoelectric properties of CoSb 3 and CoSb 3/SiC composites prepared by mechanical alloying and microwave sintering, J. Mater. Sci. Mater. Electron. 28 (2017) 10509–10515.
[38] P.-a. Zong, R. Hanus, M. Dylla, Y. Tang, J. Liao, Q. Zhang, G.J. Snyder, L. Chen, Skutterudite with graphene-modified grain-boundary complexion enhances zT enabling high-efficiency thermoelectric device, Energy Environ. Sci. 10 (2017) 183–191.
[39] A. Gharleghi, Y. Liu, M. Zhou, J. He, T.M. Tritt, C.-J. Liu, Enhancing the thermoelectric performance of nanosized CoSb 3 via short-range percolation of electrically conductive WTe 2 inclusions, J. Mater. Chem. 4 (2016) 13874–13880.
[40] C. Zhou, J. Sakamoto, D. Morelli, X. Zhou, G. Wang, C. Uher, Thermoelectric properties of Co0. 9Fe0. 1Sb3-based skutterudite nanocomposites with FeSb2 nanoinclusions, J. Appl. Phys. 109 (2011), 063722.
[41] A. Gharleghi, P.-C. Hung, F.-H. Lin, C.-J. Liu, Enhanced ZT of in x Co4Sb12–InSb nanocomposites fabricated by hydrothermal synthesis combined with solid–vapor reaction: a signature of phonon-glass and electron-crystal materials, ACS Appl. Mater. Interfaces 8 (2016) 35123–35131.
[42] A. Gharleghi, Y.-H. Pai, F.-H. Lin, C.-J. Liu, Low thermal conductivity and rapid synthesis of n-type cobalt skutterudite via a hydrothermal method, J. Mater. Chem. C 2 (2014) 4213–4220.
[43] C.-A. Wu, K.-C. Chang, F.-H. Lin, Z.-R. Yang, A. Gharleghi, T.-Z. Wei, C.-J. Liu, Low thermal conductivity and enhanced zT values of porous and nanostructured $Cu_{1-x}Ni_x$ alloys, Chem. Eng. J. 368 (2019) 409–416.
[44] A. Nozariasbmarz, J.S. Krasinski, D. Vashaee, N-type bismuth telluride nanocomposite materials optimization for thermoelectric generators in wearable applications, Materials 12 (2019) 1529.
[45] Y. Dong, G.S. Nolas, X. Zeng, T.M. Tritt, High temperature thermoelectric properties of Ba x Yb y Fe 3 CoSb 12 p-type skutterudites, J. Mater. Res. 30 (2015) 2558–2563.
[46] C.J. Giunta, Dulong And Petit, A case OF data fabrication? Bull. Hist. Chem 27 (2002) 63.
[47] J. Leitner, P. Voňka, D. Sedmidubský, P. Svoboda, Application of Neumann–Kopp rule for the estimation of heat capacity of mixed oxides, Thermochim. Acta 497 (2010) 7–13.
[48] J.S. Dyck, W. Chen, J. Yang, G.P. Meisner, C. Uher, Effect of Ni on the transport and magnetic properties of Co 1– x Ni x Sb 3, Phys. Rev. B 65 (2002) 115204.
[49] J. Yang, M. Endres, G. Meisner, Valence of Cr in skutterudites: electrical transport and magnetic properties of Cr-doped CoSb 3, Phys. Rev. B 66 (2002), 014436.
[50] J. Martin, L. Wang, L. Chen, G. Nolas, Enhanced Seebeck coefficient through energy-barrier scattering in PbTe nanocomposites, Phys. Rev. B 79 (2009) 115311.
[51] J.Y. Seto, The electrical properties of polycrystalline silicon films, J. Appl. Phys. 46 (1975) 5247–5254.
[52] S. Choi, K. Kurosaki, G. Li, Y. Ohishi, H. Muta, S. Yamanaka, S. Maeshima, Enhanced thermoelectric properties of Ga and in Co-added CoSb3-based skutterudites with optimized chemical composition and microstructure, AIP Adv. 6 (2016) 125015.
[53] J.-H. Bahk, A. Shakouri, Minority carrier blocking to enhance the thermoelectric figure of merit in narrow-band-gap semiconductors, Phys. Rev. B 93 (2016) 165209.
[54] R. Guo, X. Wang, B. Huang, Thermal conductivity of skutterudite CoSb 3 from first principles: substitution and nanoengineering effects, Sci. Rep. 5 (2015) 7806.
[55] A.M. Limarga, D.R. Clarke, The grain size and temperature dependence of the thermal conductivity of polycrystalline, tetragonal yttria-stabilized zirconia, Appl. Phys. Lett. 98 (2011) 211906.